Environmental Pollution 399 (2026) 128147

Contents lists available at ScienceDirect

Environmental Pollution

journal homepage: www.elsevier.com/locate/envpol

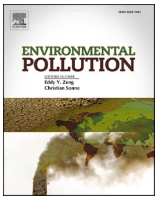

Facet and crystallinity-dependent transformation of lepidocrocite impacts cadmium redistribution

Meiling Yin [a,b], Jin Wang [b], Songxiong Zhong [c], Xiaofei Li [d], Fei Huang [e], Chen Yang [a], Fangbai Li [c], Zhi Dang [a], Chuling Guo [a,*]

[a] *School of Environment and Energy, South China University of Technology, Guangzhou 510006, China*
[b] *School of Environmental Science and Engineering, Guangzhou University, Guangzhou 510006, China*
[c] *National-Regional Joint Engineering Research Center for Soil Pollution Control and Remediation in South China, Guangdong Key Laboratory of Integrated Agro-environmental Pollution Control and Management, Institute of Eco-environmental and Soil Sciences, Guangdong Academy of Sciences, Guangzhou 510650, China*
[d] *School of Environmental and Chemical Engineering, Foshan University, 528000, Foshan, China*
[e] *Guangdong Key Laboratory of Environmental Catalysis and Health Risk Control, School of Environmental Science and Engineering, Institute of Environmental Health and Pollution Control, Guangdong University of Technology, Guangzhou, 510006, China*

ARTICLE INFO

Keywords:
Iron mineral
Fe(II)
Intrinsic properties
Transformation mechanism
Heavy metal

ABSTRACT

In redoximorphic soils and sediments, cadmium (Cd) fate is governed by Fe(II)-induced transformation of metastable iron oxides. Lepidocrocite (Lep), a ubiquitous intermediate in such environments, commonly exhibits plate-like (P-Lep) or rod-like (R-Lep) morphologies with distinct exposed facet ratios and crystallinity. These structural variations engender differential Fe(II) adsorption affinities and electron transfer capacities, thereby influencing mineralogical transformation pathways and associated Cd redistribution. Herein, we investigated the transformation of Cd-adsorbed P-Lep and R-Lep under Fe(II) concentrations of 0.2–5.0 mM using synchrotron radiation X-ray diffraction, Mössbauer spectroscopy, high-resolution transmission electron microscopy and Cd speciation extraction. At 0.2–1.0 mM Fe(II), R-Lep readily transformed into magnetite due to its enhanced Fe(II) adsorption affinity, whereas at 2.0–5.0 mM, P-Lep exhibited preferential transformation arising from its superior electron transfer capacity. Mineralogical analysis revealed that P-Lep and R-Lep transformed into magnetite primarily through dissolution-reprecipitation and topotactic transformation, respectively. Notably, magnetite formed via topotactic transformation exhibited superior Cd immobilization capacity, whereas the homoepitaxial growth of Lep facilitated Cd migration. These findings provide a mechanistic foundation for predicting Cd mobility in redox-fluctuating environments, facilitating targeted remediation strategies utilizing iron oxides.

1. Introduction

Cadmium (Cd), a highly mobile and carcinogenic metal, is prevalent in the groundwater, anaerobic subsurface water, sediments, and flooded soils contaminated by acid mine drainage (Godt et al., 2006; Wang et al., 2019; Zheng et al., 2023). In the above scenarios, the fate of Cd is closely related to the reductive transformation of iron mineral induced by Fe(II) (Shi et al., 2021; Huang et al., 2021). Besides being adsorbed on iron mineral (Shi et al., 2021), Cd can also be incorporated into the structure of crystalline iron mineral during metastable iron mineral transformation (Li et al., 2019; Yin et al., 2016). For example, the transformation of ferrihydrite into goethite (Goe) (Liu et al., 2019), magnetite (Mag) (Qiu et al., 2023), and hematite (Qu et al., 2022) is known to sequester Cd via structural incorporation, reducing Cd mobility. Thus, elucidating the impact of Cd-adsorbed metastable iron mineral transformation on Cd redistribution, especially the pivotal mechanism governing the structural incorporation of Cd into crystalline minerals, is crucial for understanding Cd geochemistry and controlling Cd mobility and biotoxicity.

Lepidocrocite (Lep, γ-FeOOH) plays a critical role as an intermediate product in the Fe(II)-mediated transformation of metastable iron minerals like ferrihydrite and can subsequently be converted into more crystalline iron minerals, such as Goe (Hansel et al., 2005; Hockmann et al., 2021; Hu et al., 2022). Consequently, Lep formation and transformation significantly influence the type and proportion of crystalline iron mineral, affecting the subsequent Cd redistribution. For example,

---

* Corresponding author.
E-mail address: clguo@scut.edu.cn (C. Guo).

https://doi.org/10.1016/j.envpol.2026.128147
Received 27 January 2026; Received in revised form 27 March 2026; Accepted 14 April 2026

Schulz et al. (2022) and Liu et al. (2022) have found that Lep experiences Oswald ripening at low Fe(II) levels (Fe(II)/Fe(III) molar ratio = 0.02) and transforms into Mag at high Fe(II) concentrations (Fe(II)/Fe (III) molar ratio = 0.2). The transformation of Lep into Goe occurs through dissolution-reprecipitation and oriented aggregation (Yan et al., 2015), whereas the formation of Mag from Lep is likely due to topotactic transformation (Yan et al., 2016). However, a recent study demonstrated that the transformation of Lep into Mag aligns with the classical nucleation theory, suggesting a dissolution-reprecipitation mechanism (Liu et al., 2022). Based on the previous research, we propose that the transformation pathway of Lep and the formation mechanism of secondary minerals vary with Fe(II) concentration. Nevertheless, identifying the Lep transformation mechanism and its impact on Cd (im) mobilization remains challenging.

Generally, Lep occurs as plate-like (P-Lep) and rod-like (R-Lep) morphologies in redoximorphic environments, with both forms resulting from the Fe(II)-mediated transformation of metastable minerals (Alekseev and Alekseeva, 2000; Fan et al., 2019). Although both P-Lep and R-Lep are dominated by {002} and {020} facets, their {002}/{020} facet ratio is different (Li et al., 2022). Minerals with a higher density of crystal facets that exhibit strong Fe(II) affinity are more susceptible to transformation (Boland et al., 2013). For instance, the transformation of Goe to Mag is more pronounced for the Goe with a higher {021} facet proportion (Usman et al., 2013). Furthermore, the differences in Fe(II) concentration, ionic strength, and Fe(II) oxidation rate during P-Lep and R-Lep formation will affect the crystallinity of Lep (Taylor, 1984; Lewis and Farmer, 1986). A recent study suggested that minerals with lower crystallinity display higher standard redox potentials, thereby undergoing more rapid transformation due to their enhanced electron transfer capacity (Liu et al., 2023). P-Lep differs from R-Lep in facet ratio ({002}/{020}) and crystallinity. Consequently, they exhibit different Fe (II) adsorption affinities and electron transfer capacities, which may influence the subsequent mineralogical transformation. However, it remains unclear how the facet ratio ({002}/{020}) and crystallinity of Lep regulate the mineralogical transformation at varying Fe(II) concentrations.

Accordingly, Cd-adsorbed P-Lep and R-Lep were synthesized in this work to investigate the effect of intrinsic properties (facet ratio and crystallinity) of Lep on mineralogical transformation and the associated Cd fate. The transformation experiments were conducted under varying Fe(II) concentrations (0.2, 1.0, 2.0, and 5.0 mM), which were commonly found in the paddy soils contaminated by acid mine drainage (Hu et al., 2022; Pan et al., 2021; Sun et al., 2015). Synchrotron radiation X-ray diffraction (SR-XRD), Mössbauer spectroscopy, high-resolution transmission electron microscopy (HRTEM), and Cd speciation extraction methods were performed to identify the newly formed secondary minerals and Cd speciation. The results will advance our understanding of how the mineralogical transformation of iron oxyhydroxides with different intrinsic properties controls the fate of Cd.

2. Materials and methods

2.1. Mineral preparation

P-Lep and R-Lep were synthesized by oxidizing Fe(II) according to the method proposed by Lewis and Farmer (1986) and Li et al. (2022). For the P-Lep preparation, 0.02 M $FeCl_2$ was first dissolved in an oxygen-free $NaNO_3$ solution (0.2 M). When the solution was adjusted to pH 6.3, natural air was introduced using a pump at a flow rate of approximately 200 mL min^{-1}. The pH value was maintained by dropwise addition of 1.0 M NaOH during the continuous supply of air. After the solution pH reached equilibrium, the air was supplied for one more hour. Then the mineral suspension was centrifuged, decanted, and washed with ultrapure water (18.2 MΩ·cm) to eliminate residual ions. Finally, the synthetic mineral was freeze-dried and analyzed using mineralogy techniques. For R-Lep, the operating conditions were modified to "0.05 M $FeCl_2$, 0.75 M $NaNO_3$, pH 6.7, and air supply rate of 100 mL min^{-1}". The remaining procedures were the same as those for P-Lep.

2.2. Transformation experiments

The transformation experiments were performed in an anaerobic glovebox (YQX-II, CIMO). First, the mineral was hydrated in a 0.05 M $NaNO_3$ solution (pH 6.5) and stirred with a magnetic rotor agitator for 24 h. For Cd-adsorbed mineral preparation, 50 μM Cd was reacted with the mineral suspension (18.0 mM Fe (III)) for 48 h. Finally, the transformation experiments (total reaction volume of 800 mL) were initiated by adding a certain volume of Fe(II) stock solution (500 mM). The final Fe(II) concentrations were set at 0.2, 1.0, 2.0, and 5.0 mM, respectively. The pH of the mineral suspension was maintained at 6.5 using an automatic titrator with 1.0 M HNO_3 or 1.0 M NaOH. All treatments were performed in triplicate. The corresponding treatments were referred to as "mineral-Fe(II) concentration". For example, the treatment with P-Lep at 0.2 mM Fe(II) was denoted as "P-Lep-0.2".

The transformation experiment lasted for 720 h. At selected reaction times, 2 mL of mineral suspensions were sampled and filtered using a 0.22 μm nylon filter for Fe(II) determination. Another 10 mL of suspension was collected for aqueous Cd determination and solid-phase Cd extraction. For mineralogy analysis, 100 mL of mineral suspensions was collected and centrifuged at 8000 rpm for 10 min. After decanting the supernatant, the solids were washed twice with 5 mM HCl to remove the adsorbed Fe(II) (Sheng et al., 2021). Then the solids were freeze-dried and preserved in the glovebox for subsequent analysis.

2.3. Elemental analysis

The aqueous Fe(II) concentration was determined by ultraviolet-visible spectrophotometry (UV-Vis, UV-2550, Shimadzu) based on the phenanthroline photometry method (Fadrus and Maly, 1975). The concentration of Cd was measured using inductively coupled plasma-mass spectrometry (ICP-MS, Thermo-Scientific X Series-2) after acidification with 2% HNO_3 (*v*/*v*). The drift correction procedure for ICP-MS followed the method described by Zhong et al. (2023). The mineral suspension was centrifuged, decanted, and used for solid-phase Cd analysis. Following the procedure proposed by Yan et al. (2021), the solid phase Cd was separated into the adsorbed Cd and coprecipitated Cd forms. The adsorbed Cd was extracted with 0.4 M HNO_3 (10 mL) for 30 min, followed by centrifugation and decantation. In succession, the remaining mineral was digested with 6.0 M HCl, diluted, and analyzed for coprecipitated Cd content.

2.4. Mineralogy analysis

The mineralogy and morphology of the synthetic Lep and secondary minerals were characterized using X-ray diffraction (XRD, Advance D8, Bruker), Fourier transform infrared spectroscopy (FTIR, VERTEX 33, Bruker), scanning electron microscopy (SEM, Merlin, ZEISS) and HRTEM (Talos F200×, Thermo Fisher). Furthermore, the corresponding fast Fourier transform (FFT) and selected area electron diffraction (SAED) in TEM were used to reveal the local crystal characteristics of poorly crystalline minerals and the overall crystal properties of well-crystalline minerals, respectively. The crystallinity of Lep was determined by calculating the relative area for crystalline peaks in the XRD pattern (Dome et al., 2020). Scanning transmission electron microscopy (STEM) was used to analyze the distribution of elements (Fe, O, and Cd) on solids. To calculate the specific surface area, samples were initially degassed at 100 °C for 16 h, followed by N_2 adsorption at 77 K, and N_2 adsorption-desorption isotherms were obtained via an Autosorb-iQ2 analyzer (Quantachrome). The specific surface area was determined using the Brunauer-Emmett-Teller (BET) method, which evaluates the amount of adsorbed N_2 on the sample surface according to multilayer adsorption theory. Surface site density of samples was obtained using potentiometric titration experiments performed on an autoburette (Metrohm). The pH was first adjusted to 3.0 using 0.1 M HCl standard solution, then titrated with 0.1 M NaOH standard solution at a rate of 0.2 mL min^{-1} until the pH stabilized at 10. Based on the acid-base titration process, the Gran function diagram was constructed to calculate the acid-base buffering capacity (H_s). Finally, the surface site density (D_s) can be calculated using Eq. 1

$$D_s = \frac{H_s N_A}{S_{BET}} \tag{1}$$

where S_{BET} represents the specific surface area of the mineral, and N_A is Avogadro's constant, which is 6.02×10^{23} (Wang et al., 2024).

Mössbauer spectra were recorded to elucidate the mineral composition and structure using a spectrometer (German, Wissel MS-500) equipped with a^{57}Co (Rh) gamma energy source (25 mCi). To avoid the superparamagnetic action of nanoparticles and the Verwey transition, Mössbauer spectra were collected at 140 K (Gorski and Scherer, 2010). After velocity calibration with the α-Fe absorber, the obtained spectra were analyzed using the Recoil software based on the Voigt-based Fitting (VBF) method (Rancourt and Ping, 1991). Mössbauer spectroscopy can determine the stoichiometry (χ) of Mag by analyzing the relative areas of $^{Tet}Fe^{3+}$ and $^{Oct}Fe^{2.5+}$ according to Eq. (2) (Gorski and Scherer, 2010):

$$x = \frac{Fe^{2+}}{Fe^{3+}} = \frac{\frac{1}{2}{}^{Oct}Fe^{2.5+}}{\frac{1}{2}{}^{Oct}Fe^{2.5+} + {}^{Tet}Fe^{3+}} \tag{2}$$

Due to the high resolution and intensity of the SR-XRD data (Natter et al., 2000), Rietveld refinement was performed on the SR-XRD data using the Pseudo-Voigt function. SR-XRD data were collected at the 14 B beamline of the Shanghai Synchrotron Radiation Facility (SSRF) using an X-ray energy of 18 keV (λ = 0.6887 Å). Diffraction patterns were recorded over 2θ = 4–34° at a step size of 0.004° and an integration time of 50 s. Unit-cell parameters (a, b, c), unit-cell volume (V) and Fe-O bond distance ($d_{Fe\text{-}O}$), together with edge-sharing ($d_{Fe\text{-}Fe(e)}$) and corner-sharing ($d_{Fe\text{-}Fe(c)}$) Fe-Fe bond distance, were determined by Rietveld refinement using Fullprof software and structural models of Lep (ICSD #27846) and Mag (ICSD #43001). Phase quantification was performed concurrently with the refinement. The average crystallite size of Lep was subsequently calculated using the Scherrer equation, based on the full width at half maximum (FWHM) and Bragg angle obtained from the Rietveld refinement (Patterson, 1939; Uvarov and Popov, 2007).

Additionally, to comprehensively elucidate the effect of Lep crystallinity and Fe(II) concentration on mineralogical transformation, the standard redox potential value (E0 H) for Fe(II)-Lep redox couple was calculated through the obtained open-circuit potential values (E_{OCP}) for P-Lep and R-Lep. The details for the Rietveld refinement in the SR-XRD data and the calculation for the average crystallite size and E0 H are given in Text S1.

3. Results and discussion

3.1. Intrinsic property of P-Lep and R-Lep

XRD characterization verified the phase purity of both original P-Lep and R-Lep, with diffraction patterns in full accordance with the lepidocrocite standard (ICSD 27846), indicating phase-pure products (Fig. 1). The relative areas of crystalline peaks in the XRD patterns showed that the crystallinity of P-Lep (41.9%) is lower than that of R-Lep (52.2%). It was demonstrated that crystallinity may influence the electron transfer capacity of minerals (Neal et al., 2003; Xu et al., 2022; Liu

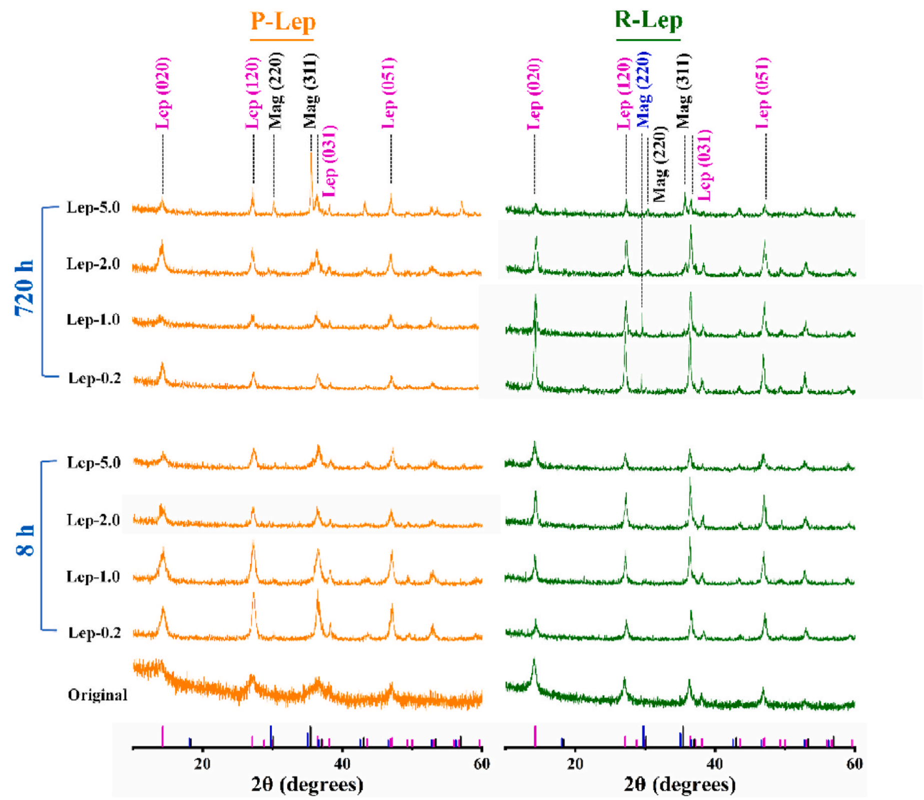

Fig. 1. The time evolution (0 h, 8 h and 720 h) of XRD patterns for plate-shaped lepidocrocite (P-Lep, orange) and rod-shaped lepidocrocite (R-Lep, olive) in the treatments with 0.2–5.0 mM Fe(II). XRD peaks associated with lepidocrocite (Lep) (ICSD #27846), {311}-predominated magnetite (Mag) (ICSD #43001), and {220}-predominated Mag (ICSD #85807) standards are shown as magenta, black, and blue bars along the x-axes, respectively. (For interpretation of the references to colour in this figure legend, the reader is referred to the Web version of this article.)

et al., 2023). Thus, E_{OCP} measurements and aqueous Fe(II) activities were employed to calculate $E0$ H values for P-Lep (1019.5 eV) and R-Lep (915.5 eV) in systems with 5.0 mM Fe(II) (Fig. S2; Table S1). The elevated $E0$ H value for P-Lep signifies greater electron transfer capacity relative to R-Lep (Liu et al., 2023).

The out-of-plane γOH vibration frequency for P-Lep (740 cm^{-1}) was red-shifted compared to R-Lep (744 cm^{-1}), indicating a smaller particle size for P-Lep (Fig. S1) (Lewis and Farmer, 1986; Xiao et al., 2017). This was corroborated by N_2 sorption measurements, which revealed a substantially higher specific surface area for P-Lep (122.2 m^2 g^{-1}) than R-Lep (58.8 m^2 g^{-1}) (Table 1). However, potentiometric titration experiments found that the surface site density of R-Lep (0.89 site·nm^{-2}) was larger than that of P-Lep (0.31 site·nm^{-2}) (Fig. S3; Table 1), suggesting superior Fe(II) adsorption capacity for R-Lep. SEM and TEM measurements provided the mean dimensional parameters (length, width and height) for P-Lep and R-Lep, enabling the construction of simplified crystal models. As shown in Fig. S4, {020} (78% of surface area) is the dominant exposed facet of P-Lep, whereas the {002} facet (54% of surface area) predominates in R-Lep. Previous studies demonstrate that {020} facets are composed of passive doubly-coordinated hydroxyl groups (Fe_2OH), whereas {002} facets are terminated by reactive hydroxyl groups, including singly coordinated (FeOH) and triply coordinated (Fe_3OH) hydroxyl groups (Ding et al., 2012; Kozin et al., 2013). Consequently, the higher surface site density and Fe(II) adsorption capacity of R-Lep originate from its greater proportion of {002} facets.

The increase in electron transfer capacity and Fe(II) adsorption capacity enhances the coupled Fe(II)-Fe(III) electron transfer and atom exchange (ETAE) efficiency, as well as labile Fe(III) formation, which is the prerequisite for secondary mineral formation (Liu et al., 2023; Boland et al., 2013). Therefore, P-Lep and R-Lep are expected to exhibit distinct transformation behaviors.

3.2. Facet/crystallinity-dependent transformation of lep

In systems with low Fe(II) concentrations (0.2 and 1.0 mM) (Fig. S7a and b), initial aqueous Fe(II) concentrations were lower in R-Lep treatments than in P-Lep treatments, reflecting the superior Fe(II) adsorption capacity of R-Lep. As reactions progressed, aqueous Fe(II) concentrations decreased, particularly in the R-Lep treatments, suggesting a greater propensity for Mag formation. After 720 h, {220} Mag diffraction peaks emerged in "R-Lep-0.2" and "R-Lep-1.0" treatments but were absent from corresponding P-Lep treatments (Fig. 1). ^{57}Fe Mössbauer spectroscopy, which exhibits exceptional sensitivity to Fe local environment changes and high precision for quantifying both amorphous and crystalline Fe phases, was employed to corroborate Mag formation (Wareppam et al., 2023; Geymond et al., 2023). As shown in Fig. 2 and Table S2, the Mössbauer spectra of Mag consist of two sextets, with the center shift of the sextet corresponding to Fe^{3+} in the tetrahedral site ($^{Tet}Fe^{3+}$ sextet) being lower than that of the sextet corresponding to Fe^{2+} and Fe^{3+} in the octahedral site ($^{Oct}Fe^{2.5+}$ sextet) (Gorski and Scherer, 2010). Based on the relative area of the two sextets, the relative abundance of Mag in the "P-Lep-0.2" and "R-Lep-0.2" treatments was determined to be 4.2% and 8.0%, respectively (Fig. 2a and b). Notably, Mag was detected by Mössbauer spectroscopy but not by the laboratory XRD in the "P-Lep-0.2" treatment. This discrepancy was likely due to the low relative content and low crystallinity of the newly formed Mag (ThomasArrigo et al., 2018; Notini et al., 2022; Geymond et al., 2023). Collectively, these findings demonstrate that R-Lep transforms more readily than P-Lep under low Fe(II) conditions. This enhanced reactivity originates from the propensity of Fe(II) to form inner-sphere surface complexes on {002} facets, facilitating interfacial electron transfer and subsequent mineralogical transformation (Usman et al., 2013). Thus, facet-dependent Fe(II) adsorption critically governs Lep transformation pathways under low Fe(II) conditions (Sheng et al., 2020).

In systems with high Fe(II) concentrations (2.0 and 5.0 mM) (Fig. S7c and d), while initial aqueous Fe(II) concentrations remained lower in R-Lep treatments, P-Lep treatments exhibited accelerated Fe(II) depletion as reactions progressed. Absolute Fe(II) consumption substantially exceeded that observed in systems with low Fe(II) concentrations. Correspondingly, {311} and {220} Mag reflections emerged in both P-Lep and R-Lep treatments after 720 h, with diffraction intensities positively correlated with Fe(II) concentration and maximal intensity observed for the "P-Lep-5.0" treatment. Phase quantification by Mössbauer spectroscopy and SR-XRD corroborated these observations. Rietveld refinement of the SR-XRD data yielded weighted profile *R*-factors (R_{wp}) below 10%, confirming reliable fit quality. Mag abundances in P-Lep treatments (19.2% at 2.0 mM; 50.3% at 5.0 mM) consistently exceeded those in corresponding R-Lep treatments (16.7% and 39.8%) (Fig. 2c and d; Fig. S5). These results collectively establish that P-Lep underwent mineralogical transformation preferentially at high Fe(II) concentrations. The reversal of relative reactivity from R-Lep dominance at low Fe(II) concentrations to P-Lep dominance at high Fe (II) concentrations suggests that transformation extent depends not merely on Fe(II) adsorption capacity, but critically on Lep crystallinity. Consistent with this, Liu et al. (2023) established that poorly crystalline iron oxyhydroxides exhibit elevated $E0$ H, facilitating Fe(III) reduction and subsequent mineralogical transformation. The higher $E0$ H of P-Lep relative to R-Lep (Table S1) becomes increasingly consequential as Fe(II) concentrations increase, as the saturation of surface adsorption sites renders electron transfer capacity the limiting factor. Consequently, crystallinity-dependent electron transfer capacity plays a crucial role in governing Lep transformation pathways under high Fe(II) concentrations.

3.3. Divergent transformation mechanism of P-Lep and R-Lep

TEM was employed to resolve the mineralogy and morphology of secondary minerals after 720 h of reaction. In the "P-Lep-0.2" treatment,

Table 1
Unit cell parameter, bond distance, average crystallite size (L), specific surface area (SSA), and surface site density (D_s) for lepidocrocite (Lep) and the secondary minerals.

Samples	P-Lep	P-Lep-0.2	P-Lep-2.0	R-Lep	R-Lep-0.2	R-Lep-2.0
a (Å)	3.887	3.877	3.880	3.881	3.877	3.878
b (Å)	12.589	12.531	12.542	12.542	12.547	12.546
c (Å)	3.083	3.074	3.076	3.075	3.075	3.074
V ($Å^3$)	150.88	149.38	149.67	149.70	149.65	149.57
$d_{Fe\text{-}O}$ (Å)	2.12 (4)	1.88 (4)	1.90 (3)	1.99 (2)	1.99 (4)	2.02 (3)
$d_{Fe\text{-}Fe(e)}$ (Å)	3.09 (3)	3.05 (3)	3.07 (2)	3.11 (3)	3.09 (3)	3.07 (1)
$d_{Fe\text{-}Fe(c)}$ (Å)	3.89 (2)	3.88 (5)	3.88 (3)	3.88 (3)	3.88 (1)	3.88 (5)
R_{wp} (%)	7.7	7.3	6.5	6.2	6.8	5.8
L (nm)	7.3	14.5	15.9	15.6	26.0	26.1
SSA ($m^2·g^{-1}$)	122.2	40.1	56.9	58.8	30.0	40.6
D_s (site·nm^{-2})	0.31	0.04	0.25	0.89	0.26	0.32

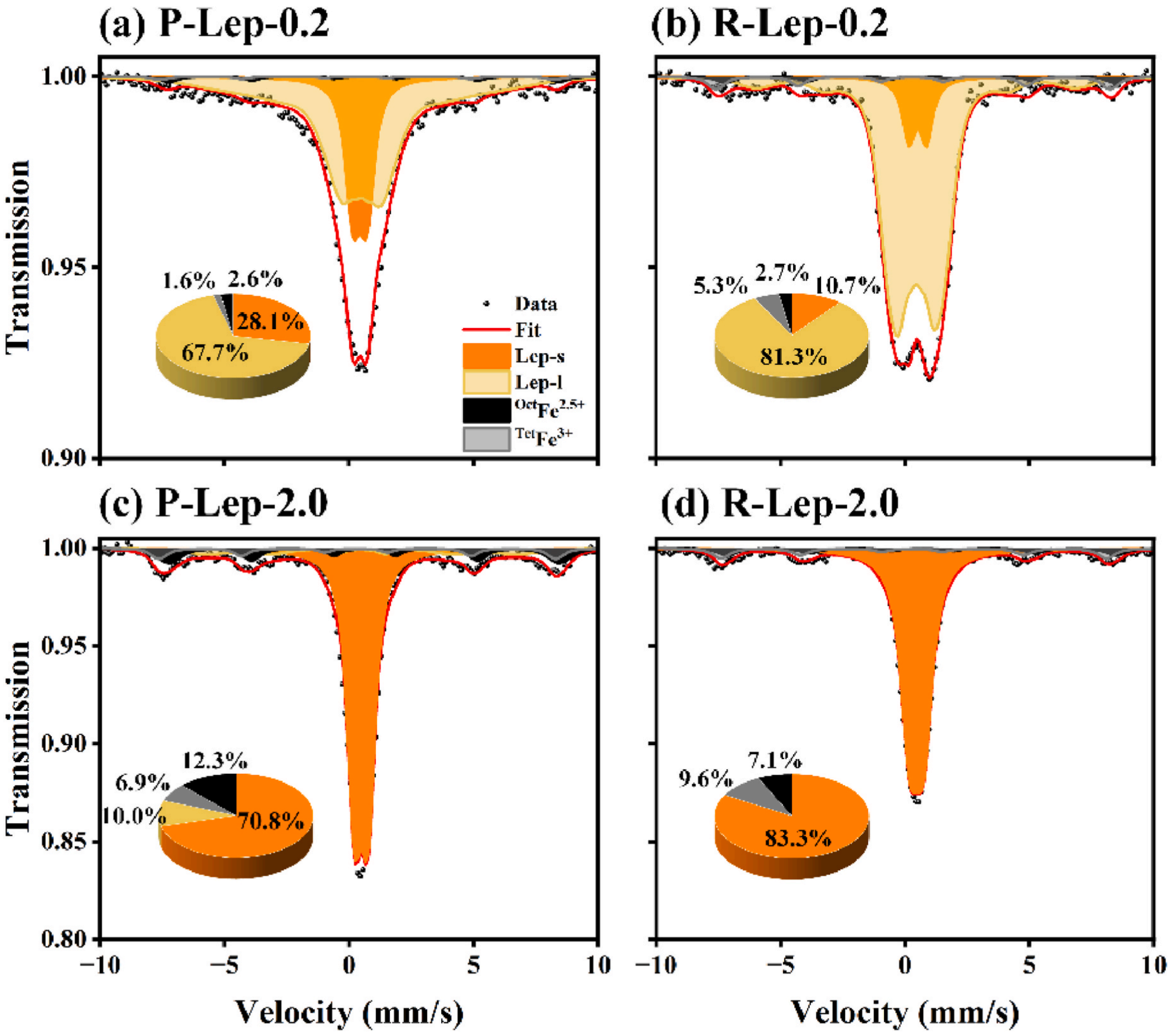

Fig. 2. Mössbauer spectra (140 K) for the secondary minerals after 720 h of reaction in the treatments with 0.2 and 2.0 mM Fe(II). The insert pie charts represent the relative abundance of secondary minerals. Lep-s and Lep-l represent Lep with small and large crystallite sizes, respectively. $^{Oct}Fe^{2.5+}$ and $^{Tet}Fe^{3+}$ denote the octahedral and tetrahedral Fe sites in Mag, respectively.

neither the Mag peak was detected in the XRD pattern nor were lattice fringes of Mag observable in the HRTEM images. However, the presence of a diffraction ring corresponding to Mag in the FFT patterns suggests the formation of Mag with low crystallinity (Fig. 3c and d). Notably, the Mag formed in the “P-Lep-0.2” treatment exhibited the {311} crystal plane and aligned along the [040] crystallographic zone axis of P-Lep (Fig. 3c and d). However, in the “R-Lep-0.2” treatment, the Mag with {220} crystal plane grew along the [00_2] crystallographic direction of R-Lep (Fig. 3a and b), consistent with the dominant {220} Mag XRD reflections (Fig. 1). The preferential growth of Mag {220} facets is attributed to their high atomic density, which confers low surface energy, high stability, and reduced free energy (Guo et al., 2004; Walls et al., 2016; Fang et al., 2022).

In systems with 2.0 mM Fe(II), the representative Mag morphology was observed in TEM images. The cubic-like Mag formed along the [040] crystallographic direction of P-Lep (Fig. 3g and h), while a multidomain cubic-like Mag was observed at the edge of R-Lep (Fig. 3e and f). These divergences in crystallographic orientation, nucleation position, and morphology of Mag are likely attributable to the distinct transformation mechanisms of P-Lep and R-Lep. It is established that the Mag formed via dissolution-reprecipitation mainly originates from labile Fe(III) (Liu et al., 2022; Sheng et al., 2020), resulting in the cubic Mag deviating from the P-Lep (Fig. 3g). A comparable finding was reported in a previous study (Liu et al., 2023). Multidomain cubic Mag has also been identified at ferrihydrite fringes, while its formation mechanism remains unclear (Hansel et al., 2005). Yang et al. (2010) demonstrated that ferrihydrite tends to undergo a topotactic process to form Mag when the release rate of the structurally reduced Fe(II) is slow. Therefore, the high crystallinity of R-Lep may contribute to its propensity for topotactic transformation, as elevated crystallinity inhibits the release of structurally reduced Fe(II). During the topotactic transformation process, Lep was transformed into Mag via dehydroxylation and atomic reorganization within its structure, without mineral dissolution (Cudennec and Lecerf, 2005). Consequently, a crystallographic orientation relationship between Mag and R-Lep was observed in the “R-Lep-0.2” treatment (Figs. 1 and 3a and b). Specifically, the preferential growth of Mag with {220} facets on R-Lep is attributed to the similarity in both angularity and dimensionality of the crystal structure of the {220} facets in Mag and that of R-Lep (Cudennec and Lecerf, 2005). Similarly, Nogueira et al. (2022) observed that Mag formation via a topotactic process demonstrates preferred orientation.

Furthermore, the results from Mössbauer spectroscopy indicated that the stoichiometry (χ) of Mag formed from the “P-Lep-0.2” and “P-Lep-2.0” treatments was 0.45 and 0.47, respectively. These values are consistent with those reported by Bu et al. (2023), who found that the Mag derived from Lep had a χ value of 0.45–0.55. In the “R-Lep-0.2” and “R-Lep-2.0” treatments, however, the χ value for the formed Mag was determined to be 0.20 and 0.27, respectively, which were much lower

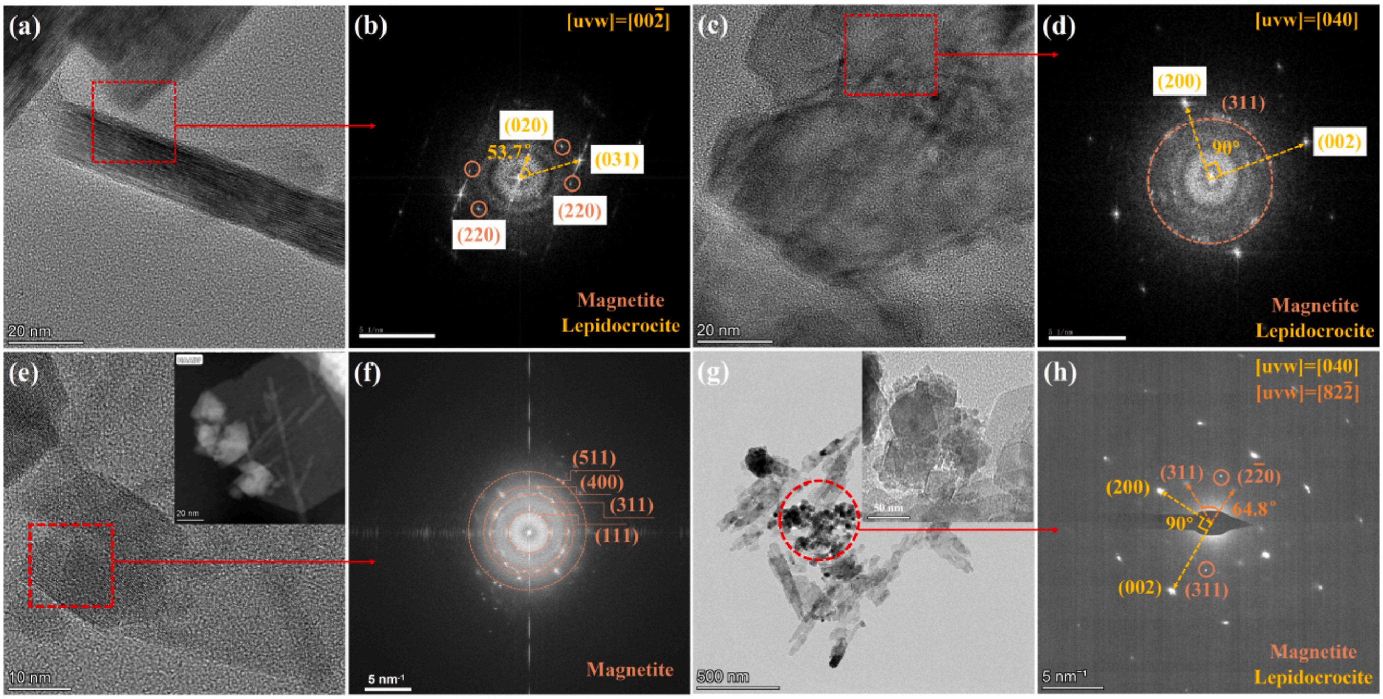

Fig. 3. Representative HRTEM micrograph and the corresponding FFT pattern of the transformation products in the (a, b) "R-Lep-0.2" treatment, (c, d) "P-Lep-0.2" treatment, and (e, f) "R-Lep-2.0" treatment; (g) TEM micrograph and the corresponding (h) SAED pattern of the transformation products in the "P-Lep-2.0" treatment; The insets in figure (e) and (g) show the representative morphology of Mag in the "R-Lep-2.0" and "P-Lep-2.0" treatments, respectively.

than that of stoichiometric Mag ($\chi = 0.5$). The result is attributed to the topotactic process during Mag formation, which suppresses Fe(II) incorporation into the Mag structure during spinel ordering (Usman et al., 2012). Overall, these results demonstrate that P-Lep transforms into Mag primarily via the dissolution-reprecipitation process, whereas the transformation of R-Lep into Mag is a topotactic process.

3.4. Effect of homoepitaxial growth on the surface property of lep

In the "P-Lep-0.2" and "P-Lep-1.0" treatments, the diffraction peaks of Lep became sharp and strong after 8 h of reaction. In the "R-Lep-0.2" and "R-Lep-1.0" treatments, however, the intensities of Lep peaks became weak after 8 h, which turned strong at 720 h (Fig. 1). Compared to the original Lep, the stronger and narrower Bragg peak of Lep after reaction with Fe(II) indicated the homoepitaxial growth of the mineral (Watari et al., 1982; Frierdich et al., 2015). Besides, the homoepitaxial growth of Lep at low Fe(II) concentrations also occurred in the research conducted by Pedersen et al. (2005) and Schulz et al. (2022). The result of the Rietveld refinement in the SR-XRD data (Fig. S6a and b) revealed that the average crystallite size of the original R-Lep was 15.6 nm, which was larger than that of P-Lep (7.3 nm) (Table 1). At 192 h, the average crystallite size of P-Lep and R-Lep increased to 14.5–15.9 nm and 26.0–26.1 nm due to the homoepitaxial growth of mineral, respectively (Table 1). Notably, the increase in crystallite size for P-Lep (98.6–117.8%) was greater than that for R-Lep (66.7%), which was due to the small crystallite size and low crystallinity of the original P-Lep. The result is consistent with the research of Southall et al. (2018), who found that the crystallite size of Goe with a low crystallinity and small particle size increased significantly during the homoepitaxial growth process. It is well established that small, low-crystallinity minerals exhibit high surface energy and numerous defects, which facilitate the dissolution of crystallites (Wang et al., 2016; Dai et al., 2017; Southall et al., 2018). The dissolution of crystallites is a prerequisite for Oswald ripening, which amplifies the size difference and promotes the labile Fe (III) enrichment in Lep particles, thereby enhancing Lep crystallite size (Dai et al., 2017; Thanh et al., 2014). After 720 h of reaction, the out-plane γOH vibration of Lep exhibited a blue shift in the FTIR spectra compared to the original Lep. Specifically, P-Lep shifted from 740 cm^{-1} to 744–746 cm^{-1}, and R-Lep shifted from 744 cm^{-1} to 748–750 cm^{-1} (Fig. S1). This result showed that the particle sizes of P-Lep and R-Lep increased after homoepitaxial growth (Xiao et al., 2017), which is consistent with the finding of Joshi and Gorski (2016), who found that Fe(II)-catalyzed recrystallization of Goe enhanced its particle size. Notably, the extent of blue shift decreased with the increase in Fe(II) concentration, suggesting that the homoepitaxial growth of Lep at lower Fe(II) concentrations resulted in a larger particle size of Lep.

In Mössbauer spectra, a superparamagnetic doublet of Lep was observed in the "R-Lep-2.0" treatment, while sextet and doublet components appeared simultaneously in the "P-Lep-2.0", "P-Lep-0.2", and "R-Lep-0.2" treatments. The co-existence of sextet and doublet components indicated significant differences in the crystallite size of Lep, which likely resulted from the homoepitaxial growth of Lep (De Grave et al., 1986; Wang et al., 2016; Southall et al., 2018). The paramagnetic fraction of the sample decreases with decreasing temperature, causing the doublet spectrum to split into a sextet (Guyodo et al., 2016). Additionally, the sample with a large crystallite size exhibits a high magnetic ordering temperature (Wang et al., 2016). Therefore, the sextet component corresponds to the mineral with a large crystallite size. The result of Mössbauer spectroscopy demonstrated that the proportion of Lep with large crystallite size in the "P-Lep-0.2" treatment (67.7 ± 4.4%) was higher than that in the "P-Lep-2.0" treatment (10.0 ± 4.3%), which further confirmed that the increase in crystallite size of Lep due to homoepitaxial growth was more pronounced at low Fe(II) concentrations than that at high Fe(II) concentrations.

In this experiment, the homoepitaxial growth of Lep altered the structure and surface properties of the mineral as well. Rietveld refinement of SR-XRD data (Fig. S6, Table 1) revealed that the cell volume and parameters (*a*, *b* and *c*) of Lep after homoepitaxial growth were smaller than those of the original Lep. Moreover, the variation of P-Lep in cell volume and parameter was more pronounced than that of R-Lep, indicating that P-Lep underwent stronger morphological alteration than R-Lep (Li et al., 2016). The previous research suggests that the growth of the {002} facet in Lep can be reflected by the variation of edge-sharing Fe-Fe bond distance ($d_{Fe\text{-}Fe(e)}$) (*a*-axis) or hydrogen bonding Fe-Fe linkage (*b*-axis), and the {020} facet depends on both $d_{Fe\text{-}Fe(e)}$ and corner-sharing Fe-Fe bond distance ($d_{Fe\text{-}Fe(c)}$) (*c*-axis) (Liao et al., 2020). In the “P-Lep-0.2” and “P-Lep-2.0” treatments, the homoepitaxial growth of Lep decreased the $d_{Fe\text{-}Fe(e)}$ and parameters *a* and *b*, while the $d_{Fe\text{-}Fe(c)}$ remained constant. In the treatments with R-Lep, $d_{Fe\text{-}Fe(e)}$ and parameter *a* slightly decreased, parameter *b* increased, and $d_{Fe\text{-}Fe(c)}$ and parameter *c* remained constant throughout the experiment. It has been proposed that the decrease in bond distance enhances the atomic density of the facet, thereby inhibiting facet growth (Kelly et al., 2012). Consequently, the homoepitaxial growth of Lep significantly suppressed the growth of the {002} facet in the treatments with P-Lep, but not in the treatments with R-Lep. The {002} facet consists of active single (FeOH, -OH) and tri-coordinate (Fe_3OH, μ3-OH) hydroxyls (Ding et al., 2012). Besides, the increase in mineral crystallite size in the treatments with P-Lep was larger than that in the treatments with R-Lep. Therefore, we hypothesize that the reduction of mineral surface site density in the treatments with P-Lep is more pronounced than that in the treatments with R-Lep.

To verify the above hypothesis, we analyzed the specific surface area and surface site density of the secondary minerals (Table 1). In the “P-Lep-0.2” treatment, the specific surface area and surface site density of the minerals after homoepitaxial growth declined to approximately one-third and one-eighth of those of the original P-Lep, respectively. In the “R-Lep-0.2” treatment, however, these values were approximately half and one-third of those of the original R-Lep, respectively. These results strongly supported the above hypothesis. Additionally, the surface site density of iron mineral is positively correlated with its heavy metal adsorption capacity (Liang et al., 2021; Xue et al., 2024). Therefore, these results also indicated that the homoepitaxial growth of Lep in the “P-Lep-0.2” treatment exerts a more significant effect on Cd repartitioning than that in the “R-Lep-0.2” treatment.

3.5. *Effect of lep homoepitaxial growth and transformation on Cd fate*

In systems with 0.2–2.0 mM Fe(II), aqueous Cd concentrations experienced an initial increase (within 1 h) in R-Lep treatments (Fig. 4). This phenomenon is attributed to the high adsorption affinity of R-Lep for Fe(II), which competes with Cd for adsorption sites on Lep (Zhao et al., 2022). As the reaction proceeded, the aqueous Cd concentration decreased before subsequently increasing. At the end of the reaction (720 h), the aqueous Cd concentration in the “R-Lep-0.2” treatment reached 17.4 μM, which was lower than that observed in the “P-Lep-0.2” treatment (29.9 μM) (Fig. 4a). In systems with 1.0 mM and 2.0 mM Fe (II), however, the final aqueous Cd concentrations in the “R-Lep-1.0” (13.5 μM) and “R-Lep-2.0” (10.4 μM) treatments were comparable to those in the “P-Lep-1.0” (14.5 μM) and “P-Lep-2.0” (15.0 μM) treatments, which were significantly lower than those in systems with 0.2 mM Fe(II) (Fig. 4b and c). The most pronounced homoepitaxial growth of Lep was observed in the “P-Lep-0.2” treatment, resulting in a significant reduction in the specific surface area and surface site density of the mineral, along with subsequent Cd release (Table 1). Previous studies have also found that Fe(II)-induced homogeneous growth of other iron minerals leads to the release of heavy metals (Latta et al., 2012). Therefore, the substantial increase in aqueous Cd concentration in the “P-Lep-0.2” treatment is attributed to the homoepitaxial growth of P-Lep.

In systems with 5.0 mM Fe(II), the aqueous Cd concentration increased significantly at the initial reaction stage due to the substantial

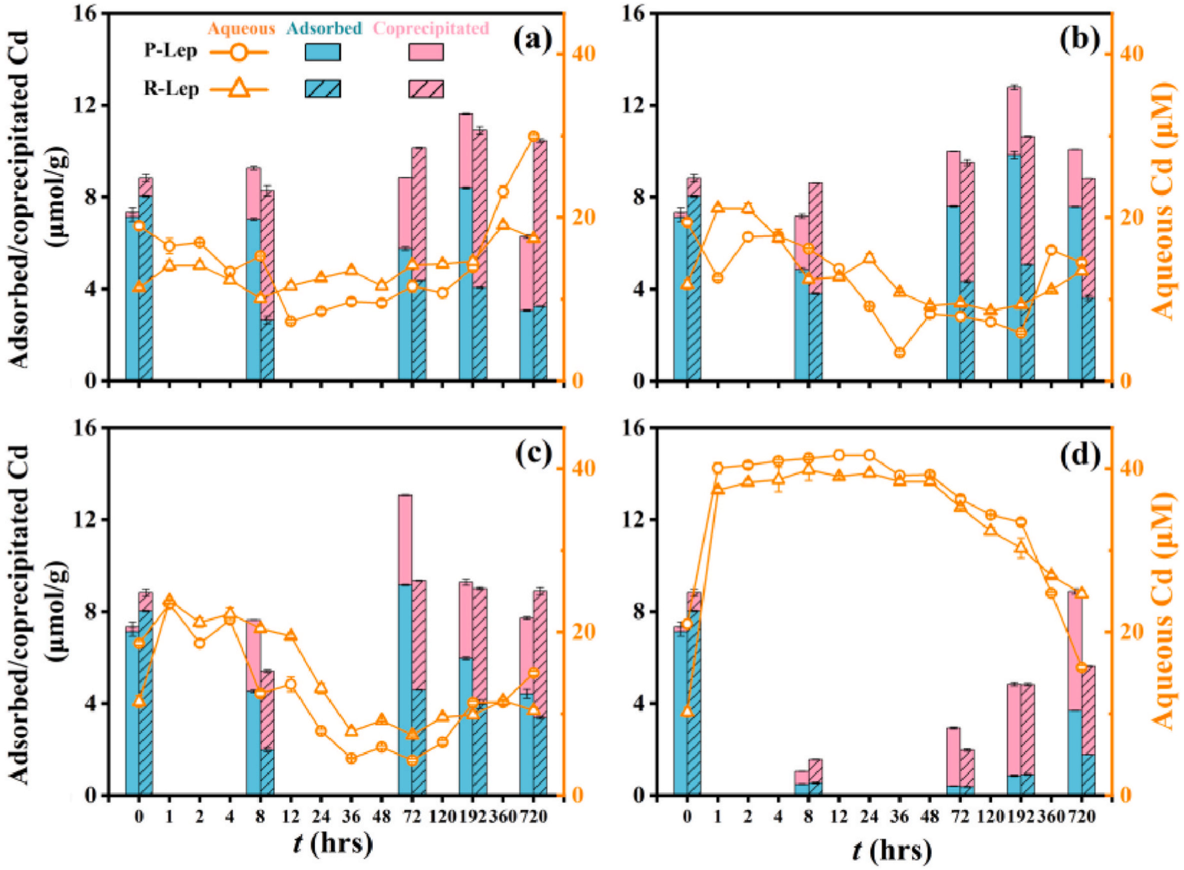

Fig. 4. Kinetics of aqueous, adsorbed, and coprecipitated Cd during the phase transformation of P-Lep and R-Lep catalyzed by (a) 0.2 mM, (b) 1.0 mM, (c) 2.0 mM, and (d) 5.0 mM Fe(II).

dissolution of Lep (Fig. 4d). Subsequently, the aqueous Cd concentrations decreased, with the final concentration in the "R-Lep-5.0" treatment exceeding that in the "P-Lep-5.0" treatment. Correspondingly, the amount of newly formed Mag was highest in the "P-Lep-5.0" treatment (Fig. 3). Mag is a crystalline iron oxide that can effectively sequestrate Cd via the adsorption and coprecipitation process (Li et al., 2020; Wang et al., 2011). Furthermore, the transformation of Lep into Mag increased the specific surface area and surface site density of the solid phase (Table 1), which positively correlated with its Cd adsorption capacity (Xue et al., 2024). Additionally, STEM mapping of secondary minerals revealed a qualitative visual enrichment of Cd on Mag (Fig. S8). Thus, the rapid decrease of aqueous Cd concentration observed in the "P-Lep-5.0" treatment is associated with the formation of Mag.

Solid-phase Cd was operationally defined as adsorbed and coprecipitated fractions based on sequential extraction procedures, with the latter representing Cd sequestered via structural substitution or physical encapsulation (Qiu et al., 2023; Yan et al., 2021). In systems with 0.2–2.0 mM Fe(II), coprecipitated Cd contents in P-Lep and R-Lep treatments increased by 2.0–2.9 and 2.6–4.8 μmol/g, respectively, compared to the initial contents after 8 h of reaction. During subsequent reaction progress, coprecipitated Cd remained relatively constant in the "P-Lep-0.2" (2.2–3.2 μmol/g), "P-Lep-1.0" (2.3–3.0 μmol/g), and "P-Lep-2.0" (3.1–3.9 μmol/g) treatments, while adsorbed Cd exhibited an initial increase followed by a decline, reaching 3.1, 7.6, and 4.4 μmol/g at 720 h, respectively (Fig. 4a, b, c). By contrast, R-Lep treatments showed continuous decreases in adsorbed Cd to 3.2, 3.6, and 3.4 μmol/g at 720 h, accompanied by progressive coprecipitated Cd accumulation to 7.2, 5.2, and 5.5 μmol/g (Fig. 4a, b, c). In systems with 5.0 mM Fe(II), both adsorbed and coprecipitated Cd contents increased continuously after 8 h (Fig. 4d). At the end of the reaction, the contents of adsorbed (3.7 μmol/g) and coprecipitated (5.2 μmol/g) Cd in the "P-Lep-5.0" treatment surpassed those in the "R-Lep-5.0" treatment (adsorbed Cd: 1.8 μmol/g; coprecipitated Cd: 3.9 μmol/g), primarily due to the notable Mag formation in the "P-Lep-5.0" treatment. Collectively, Fe(II)-induced transformation of Lep substantially increased coprecipitated Cd content, thereby enhancing Cd stability.

Previous studies have demonstrated that Cd incorporation into Mag occurs via Fe(III)/Fe(II) substitution (Shi et al., 2021) and/or physical encapsulation (Zhou et al., 2020). Consequently, the amount of newly formed Mag was expected to correlate positively with coprecipitated Cd content. However, in systems with 0.2–2.0 mM Fe(II), incorporated Cd increased substantially during R-Lep transformation, whereas P-Lep treatments showed minimal variation. Notably, R-Lep-2.0 yielded less Mag than P-Lep-2.0, contradicting the expected trend (Fig. 4c). Structural Cd incorporation is known to reduce the hyperfine magnetic field distribution of minerals (Bu et al., 2023; Huang et al., 2020). Accordingly, R-Lep-2.0 exhibited a lower hyperfine magnetic field distribution for $^{\mathrm{Tet}}\mathrm{Fe}^{3+}$ (480.75 kOe) and $^{\mathrm{Oct}}\mathrm{Fe}^{2.5+}$ (484.14 kOe) compared to P-Lep-2.0 ($^{\mathrm{Tet}}\mathrm{Fe}^{3+}$: 494.51 kOe; $^{\mathrm{Oct}}\mathrm{Fe}^{2.5+}$: 486.66 kOe) (Table S2). These data indicate that Mag derived from R-Lep sequestered Cd more efficiently via lattice substitution than that from P-Lep. This disparity is attributed to the topotactic transformation mechanism operative in R-Lep treatments, which proceeds via solid-state atomic rearrangement without dissolution, thereby retaining Cd within the precursor structure and facilitating its incorporation into the product Mag lattice.

3.6. *Environmental implication*

Lep is a crucial intermediate for crystalline iron oxides transformed from metastable iron minerals. This study demonstrated that Lep properties (facet ratio and crystallinity) profoundly influence mineralogical transformation and concurrent Cd redistribution. At low Fe(II) concentrations, poorly crystalline Lep preferentially undergoes homoepitaxial growth, which facilitates Cd mobilization. However, at high Fe(II) concentrations, it is more likely to transform into Mag, thereby enhancing Cd sequestration through adsorption. Notably, highly crystalline Lep favors Mag formation via topotactic transformation. The resulting Mag can immobilize Cd within its structure more effectively than that formed from poorly crystalline Lep through dissolution–reprecipitation, thereby enhancing the stability of Cd. Given the similarity in composition and structure between Lep and other iron minerals, this study provides new insights into the transformation mechanisms of the same mineral exhibiting different properties and their impacts on heavy metal redistribution, which is of great significance for the use of iron minerals in the remediation of heavy metal pollution in redox-fluctuating environments.

4. Conclusion

In this study, the effects of mineral properties (facet and crystallinity) on Lep transformation and associated Cd redistribution were systematically investigated. The results demonstrated that the influence of mineral properties on Lep transformation into Mag varies with increasing Fe(II) concentrations. At low Fe(II) concentrations (Fe(II)/Fe(III) molar ratios = 0.01–0.06), the facet-dependent Fe(II) adsorption capacity of Lep exerted a dominant control on the transformation process. At high Fe(II) concentrations (Fe(II)/Fe(III) molar ratios = 0.1–0.3), the electron transfer capacity, which is crystallinity-dependent, assumed greater importance during mineralogical transformation. Low Fe(II) concentrations promoted homoepitaxial growth of Lep and enhanced Cd migration, while high Fe(II) concentrations encouraged the transformation of Lep into Mag and increased Cd stability. The transformation pathway of Lep is crucial for Cd bioavailability in natural environments. Furthermore, the divergent transformation mechanisms for Lep with distinct properties were elucidated. The transformation of P-Lep into Mag proceeded primarily via dissolution-reprecipitation, whereas Mag formation from R-Lep occurred through a topotactic process. The Mag produced from P-Lep and R-Lep exhibited differences in morphology and stoichiometry, accounting for variations in Cd immobilization capacity. Notably, Mag formed via topotactic transformation demonstrated superior Cd incorporation within its structure, thereby enhancing Cd stability. These findings demonstrate that Lep transformation mechanisms and Cd (im)mobilization are governed by mineral properties, thereby advancing our understanding of heavy metal behavior constrained by iron minerals in redoximorphic environments.

CRediT authorship contribution statement

Meiling Yin: Writing – review & editing, Writing – original draft, Validation, Methodology, Formal analysis, Data curation, Conceptualization. **Jin Wang:** Writing – review & editing, Visualization, Validation, Methodology, Conceptualization. **Songxiong Zhong:** Writing – review & editing, Validation, Methodology, Conceptualization. **Xiaofei Li:** Writing – review & editing, Methodology, Investigation, Data curation. **Fei Huang:** Writing – review & editing, Validation, Methodology, Data curation. **Chen Yang:** Writing – review & editing, Supervision, Methodology, Investigation. **Fangbai Li:** Writing – review & editing, Resources, Methodology, Conceptualization. **Zhi Dang:** Writing – review & editing, Supervision, Resources, Funding acquisition, Conceptualization. **Chuling Guo:** Writing – review & editing, Supervision, Resources, Project administration, Methodology, Funding acquisition, Conceptualization.

Declaration of competing interest

The authors declare that they have no known competing financial interests or personal relationships that could have appeared to influence the work reported in this paper.

Acknowledgements

This work was supported by the Guangdong Natural Science

Foundation (No. 2024A1515010861) and the National Key Research and Development Program of China (No. 2023YFC3207300).

Appendix A. Supplementary data

Supplementary data to this article can be found online at https://doi.org/10.1016/j.envpol.2026.128147.

Data availability

Data will be made available on request.

References

Alekseev, A.O., Alekseeva, T.V., 2000. On the lepidocrocite formation in soils. Eurasian Soil Sci. 33, 1053–1060.

Boland, D.D., Collins, R.N., Glover, C.J., Waite, T.D., 2013. An in situ quick-EXAFS and redox potential study of the Fe(II)-catalysed transformation of ferrihydrite. Colloids Surf., A 435 (20), 2–8.

Bu, H., Lei, Q., Tong, H., Liu, C., Hu, S., Xu, W., Wang, Y., Chen, M., Qiao, J., 2023. Humic acid controls cadmium stabilization during Fe(II)-induced lepidocrocite transformation. Sci. Total Environ. 861, 160624.

Cudennec, Y., Lecerf, A., 2005. Topotactic transformations of goethite and lepidocrocite into hematite and maghemite. Solid State Sci. 7, 520–529.

Dai, C., Lin, M., Hu, Y., 2017. Heterogeneous Ni- and Cd-bearing ferrihydrite precipitation and recrystallization on quartz under acidic pH condition. ACS Earth Space Chem. 1, 621–628.

De Grave, E., Persoons, R.M., Chambaere, D.G., Vandenberghe, R.E., Bowen, L.H., 1986. An ^{57}Fe Mössbauer effect study of poorly crystalline γ-FeOOH. Phys. Chem. Miner. 13, 61–67.

Ding, X., Song, X., Boily, J.-F., 2012. Identification of fluoride and phosphate binding sites at FeOOH surfaces. J. Phys. Chem. C 116, 21939–21947.

Dome, K., Podgorbunskikh, E., Bychkov, A., Lomovsky, O., 2020. Changes in the crystallinity degree of starch having different types of crystal structure after mechanical pretreatment. Polymers 12, 641.

Fan, C., Guo, C.L., Chen, M.Q., Huang, W.L., Wan, J.J., Reinfelder, J.R., Li, X.F., Zeng, Y. F., Lu, G.N., Dang, Z., 2019. Transformation of cadmium-associated schwertmannite and subsequent element repartitioning behaviors. Environ. Sci. Pollut. Res. 26, 617–627, 2019.

Fang, Z., Yan, N., Liu, S.Frank, 2022. Modulating preferred crystal orientation for efficient and stable perovskite solar cells—From progress to perspectives. InfoMat 4, e12369.

Fadrus, H., Maly, J., 1975. Suppression of iron (III) interference in the determination of iron (II) in water by the 1, 10-phenanthroline method. Analyst 100, 549–554.

Friedrich, A.J., Helgeson, M., Liu, C., Wang, C., Rosso, K.M., Scherer, M.M., 2015. Iron atom exchange between hematite and aqueous Fe(II). Environ. Sci. Technol. 49, 8479–8486.

Geymond, U., Briolet, T., Combaudon, V., Sissmann, O., Martinez, I., Duttine, M., Moretti, I., 2023. Reassessing the role of magnetite during natural hydrogen generation. Front. Earth SC-SWITZ 11.

Godt, J., Scheidig, F., Grosse-Siestrup, C., Esche, V., Brandenburg, P., Reich, A., Groneberg, D.A., 2006. The toxicity of cadmium and resulting hazards for human health. J. Occup. Med. Toxicol. 1, 22.

Gorski, C.A., Scherer, M.M., 2010. Determination of nanoparticulate magnetite stoichiometry by Mossbauer spectroscopy, acidic dissolution, and powder X-ray diffraction: a critical review. Am. Mineral. 95, 1017–1026.

Guo, X., Sasaki, Y., Kashiwaya, Y., Ishii, K., 2004. Microreaction mechanism in reduction of magnetite to wustite. Metall. Mater. Trans. B 35, 517–522.

Guyodo, Y., Bonville, P., Till, J.L., Ona-Nguema, G., Lagroix, F., Menguy, N., 2016. Constraining the origins of the magnetism of lepidocrocite (γ-FeOOH): a mössbauer and magnetization study. Front. Earth Sci. 4.

Hansel, C.M., Benner, S.G., Fendorf, S., 2005. Competing Fe(II)-induced mineralization pathways of ferrihydrite. Environ. Sci. Technol. 39, 7147–7153.

Hockmann, K., Karimian, N., Schlagenhauff, S., Planer-Friedrich, B., Burton, E.D., 2021. Impact of antimony(V) on iron(II)-catalyzed ferrihydrite transformation pathways: a novel mineral switch for feroxyhyte formation. Environ. Sci. Technol. 55 (8), 4954–4963.

Hu, S., Zhen, L., Liu, S., Liu, C., Shi, Z., Li, F., Liu, T., 2022. Synchronous sequestration of cadmium and fulvic acid by secondary minerals from Fe(II)-catalyzed ferrihydrite transformation. Geochem. Cosmochim. Acta 334, 83–98.

Huang, H., Wang, J., Yao, R., Bostick, B.C., Prommer, H., Liu, X., Sun, J., 2020. Effects of divalent heavy metal cations on the synthesis and characteristics of magnetite. Chem. Geol. 547, 119669.

Huang, J., Jones, A., Waite, T.D., Chen, Y., Huang, X., Rosso, K.M., Kappler, A., Mansor, M., Tratnyek, P.G., Zhang, H., 2021. Fe(II) redox chemistry in the environment. Chem. Rev. 121, 8161–8233.

Joshi, P., Gorski, C.A., 2016. Anisotropic morphological changes in goethite during Fe^{2+}-catalyzed recrystallization. Environ. Sci. Technol. 50, 7315–7324.

Kelly, A., Knowles, K.M., 2012. Crystallography and Crystal Defects. John Wiley & Sons.

Kozin, P.A., Shchukarev, A., Boily, J.F., 2013. Electrolyte ion binding at iron oxyhydroxide mineral surfaces. Langmuir 29, 12129–12137.

Latta, D.E., Gorski, C.A., Scherer, M.M., 2012. Influence of Fe^{2+}-catalysed iron oxide recrystallization on metal cycling. Biochem. Soc. Trans. 40, 1191–1197.

Lewis, D.G., Farmer, V.C., 1986. Infrared absorption of surface hydroxyl groups and lattice vibrations in lepidocrocite (γ-FeOOH) and boehmite (γ-AlOOH). Clay Miner. 21 (1), 93–100.

Li, W., Liang, X., An, P., Feng, X., Tan, W., Qiu, G., Yin, H., Liu, F., 2016. Mechanisms on the morphology variation of hematite crystals by Al substitution: the modification of Fe and O reticular densities. Sci. Rep. 6, 35960.

Li, X., Guo, C., Jin, X., Yao, Q., Liu, Q., Zhang, L., Lu, G., Reinfelder, J.R., Huang, W., Dang, Z., 2022. Molecular-scale study of Cr(VI) adsorption onto lepidocrocite facets by EXAFS, in situ ATR-FTIR, theoretical frequency calculations and DFT+U techniques. Environ. Sci. Nano 9, 568–581.

Li, X., Yang, Z., Zhang, C., Wei, J., Zhang, H., Li, Z., Ma, C., Wang, M., Chen, J., Hu, J., 2019. Effects of different crystalline iron oxides on immobilization and bioavailability of Cd in contaminated sediment. Chem. Eng. J. (Amsterdam, Neth.) 373, 307–317.

Li, Y., Wei, G., Liang, X., Zhang, C., Zhu, J., Arai, Y., 2020. Metal substitution-induced reducing capacity of magnetite coupled with aqueous Fe(II). ACS Earth Space Chem. 4, 905–911.

Liang, Y., Jin, J., Xiang, Y., Wang, M., Xiong, J., Hou, J., Tan, W., 2021. Insights into the improving mechanism of defect-mediated As(V) adsorption on hematite nanoplates. Chemosphere 280, 130597.

Liao, S., Wang, X., Yin, H., Post, J.E., Yan, Y., Tan, W., Huang, Q., Liu, F., Feng, X., 2020. Effects of Al substitution on local structure and morphology of lepidocrocite and its phosphate adsorption kinetics. Geochem. Cosmochim. Acta 276, 109–121.

Liu, J., Sheng, A., Li, X., Arai, Y., Ding, Y., Nie, M., Yan, M., Rosso, K.M., 2022. Understanding the importance of labile Fe(III) during Fe(II)-catalyzed transformation of metastable iron oxyhydroxides. Environ. Sci. Technol. 56, 3801–3811.

Liu, L., Wang, X., Zhu, M., Ma, J., Zhang, J., Tan, W., Feng, X., Yin, H., Liu, F., 2019. The speciation of Cd in Cd–Fe coprecipitates: does Cd substitute for Fe in goethite structure? ACS Earth Space Chem. 3, 2225–2236.

Liu, Y., Ding, Y., Sheng, A., Li, X., Chen, J., Arai, Y., Liu, J., 2023. Fe(II)-Catalyzed transformation of ferrihydrite with different degrees of crystallinity. Environ. Sci. Technol. 57 (17), 6934–6943.

Natter, H., Schmelzer, M., Löffler, M.-S., Krill, C.E., Fitch, A., Hempelmann, R., 2000. Grain-growth kinetics of nanocrystalline iron studied in situ by synchrotron real-time X-ray diffraction. J. Phys. Chem. B 104, 2467–2476.

Neal, A.L., Rosso, K.M., Geesey, G.G., Gorby, Y.A., Little, B.J., 2003. Surface structure effects on direct reduction of iron oxides by Shewanella oneidensis. Geochem. Cosmochim. Acta 67, 4489–4503.

Nogueira, V.M., Barbosa, P.F., Mayanna, S., Silva, A.M., Toledo, C.L.B., Lagoeiro, L.E., Assis, L.M., 2022. Characterization of the crystallographic preferred orientation relationships of the magnetite-hematite-goethite phase transformation during martitization. Minerals 12, 326.

Notini, L., ThomasArrigo, L.K., Kaegi, R., Kretzschmar, R., 2022. Coexisting goethite promotes Fe(II)-catalyzed transformation of ferrihydrite to goethite. Environ. Sci. Technol. 56, 12723–12733.

Pan, Y., Chen, J., Gao, K., Lu, G., Ye, H., Wen, Z., Dang, Z., 2021. Spatial and temporal variations of Cu and Cd mobility and their controlling factors in pore water of contaminated paddy soil under acid mine drainage: a laboratory column study. Sci. Total Environ. 792, 148523.

Patterson, A.L., 1939. The scherrer formula for X-Ray particle size determination. Phys. Rev. 56, 978–982.

Pedersen, H.D., Postma, D., Jakobsen, R., Larsen, O., 2005. Fast transformation of iron oxyhydroxides by the catalytic action of aqueous Fe(II). Geochem. Cosmochim. Acta 69, 3967–3977.

Qiu, J., Hou, X., Ren, Y., Liu, C., Meng, F., Lee, J.-F., Lin, Y., Huang, Z., Ma, H., Shi, Z., Feng, C., 2023. Photoinduced transformation of ferrihydrite in the presence of aqueous sulfite and its influence on the repartitioning of Cd. Water Res. 231, 119607.

Qu, C., Chen, J., Mortimer, M., Wu, Y., Cai, P., Huang, Q., 2022. Humic acids restrict the transformation and the stabilization of Cd by iron (hydr)oxides. J. Hazard. Mater. 430, 128365.

Rancourt, D., Ping, J., 1991. Voigt-based methods for arbitrary-shape static hyperfine parameter distributions in mössbauer spectroscopy. Nucl. Instrum. Methods Phys. Res. B 58, 85–97.

Schulz, K., ThomasArrigo, L.K., Kaegi, R., Kretzschmar, R., 2022. Stabilization of ferrihydrite and lepidocrocite by silicate during Fe(II)-catalyzed mineral transformation: impact on particle morphology and silicate distribution. Environ. Sci. Technol. 56 (9), 5929–5938.

Sheng, A., Liu, J., Li, X., Luo, L., Ding, Y., Chen, C., Zhang, X., Wang, C., Rosso, K.M., 2021. Labile Fe(III) supersaturation controls nucleation and properties of product phases from Fe(II)-catalyzed ferrihydrite transformation. Geochem. Cosmochim. Acta 309, 272–285.

Sheng, A., Liu, J., Li, X., Oafoku, O., Collins, R.N., Jones, A.M., Pearce, C.I., Wang, C., Ni, J., Lu, A., Rosso, K.M., 2020. Labile Fe(III) from sorbed Fe(II) oxidation is the key intermediate in Fe(II)-catalyzed ferrihydrite transformation. Geochem. Cosmochim. Acta 272, 105–120.

Shi, M., Min, X., Ke, Y., Lin, Z., Yang, Z., Wang, S., Peng, N., Yan, X., Luo, S., Wu, J., Wei, Y., 2021. Recent progress in understanding the mechanism of heavy metals retention by iron (oxyhydr)oxides. Sci. Total Environ. 752, 141930.

Southall, S.C., Micklethwaite, S., Wilson, S., Frierdich, A.J., 2018. Changes in crystallinity and tracer-Isotope distribution of goethite during Fe(II)-accelerated recrystallization. ACS Earth Space Chem. 2, 1271–1282.

Sun, M., Xiao, T., Ning, Z., Xiao, E., Sun, W., 2015. Microbial community analysis in rice paddy soils irrigated by acid mine drainage contaminated water. Appl. Microbiol. Biotechnol. 99, 2911–2922.

Taylor, R.M., 1984. Influence of chloride on the formation of iron oxides from Fe(II) chloride. II. Effect of [cl] on the formation of lepidocrocite and its crystallinity. Clays Clay Miner. 32, 175–180.

Thanh, N.T.K., Maclean, N., Mahiddine, S., 2014. Mechanisms of nucleation and growth of nanoparticles in solution. Chem. Rev. 114, 7610–7630.

ThomasArrigo, L.K., Byrne, J.M., Kappler, A., Kretzschmar, R., 2018. Impact of organic matter on iron(II)-catalyzed mineral transformations in ferrihydrite–organic matter coprecipitates. Environ. Sci. Technol. 52, 12316–12326.

Uvarov, V., Popov, I., 2007. Metrological characterization of X-ray diffraction methods for determination of crystallite size in nano-scale materials. Mater. Charact. 58, 883–891.

Usman, M., Abdelmoula, M., Hanna, K., Grégoire, B., Faure, P., Ruby, C., 2012. Fe^{II} induced mineralogical transformations of ferric oxyhydroxides into magnetite of variable stoichiometry and morphology. J. Solid State Chem. 194, 328–335.

Usman, M., Abdelmoula, M., Faure, P., Ruby, C., Hanna, K., 2013. Transformation of various kinds of goethite into magnetite: effect of chemical and surface properties. Geoderma 197–198, 9–16.

Walls, B., Lübben, O., Palotás, K., Fleischer, K., Walshe, K., Shvets, I.V., 2016. Oxygen vacancy induced surface stabilization: (110) terminated magnetite. Phys. Rev. B 94, 165424.

Wang, C., Chen, K., Yin, M., Zhou, Y., Zhuang, Q., Cao, Q., Dang, Z., Guo, C., 2024. Surface properties of schwertmannite with different sulfate contents and its effect on Cr(VI) adsorption. Geochem. Cosmochim. Acta 373, 245–258.

Wang, X., Zhu, M., Koopal, L.K., Li, W., Xu, W., Liu, F., Zhang, J., Liu, Q., Feng, X., Sparks, D.L., 2016. Effects of crystallite size on the structure and magnetism of ferrihydrite. Environ. Sci. Nano 3, 190–202.

Wang, X.S., Liu, F., Lu, H.J., Zhang, P., Zhou, H.Y., 2011. Adsorption kinetics of Cd(II) from aqueous solution by magnetite. Desalination Water Treat. 36, 203–209.

Wang, Y., Dong, R., Zhou, Y.Z., Luo, X., 2019. Characteristics of groundwater discharge to river and related heavy metal transportation in a ountain mining area of Dabaoshan, southern China. Sci. Total Environ. 679, 346–358.

Wareppam, B., Kuzmann, E., Garg, V.K., Singh, L.H., 2023. Mössbauer spectroscopic investigations on iron oxides and modified nanostructures: a review. J. Mater. Res. 38, 937–957.

Watari, F., Landuyt, J., Delavignette, P., Amelinckx, S., Igata, N., 1982. X-Ray peak broadening as a result of twin formation in some oxides derived by dehydration. Phys. Status Solidi 73, 215–224.

Xiao, W., Jones, A.M., Collins, R.N., Bligh, M.W., Waite, T.D., 2017. Use of fourier transform infrared spectroscopy to examine the Fe(II)-Catalyzed transformation of ferrihydrite. Talanta 175, 30–37.

Xu, Z., Yu, Y., Xu, X., Tsang, D.C.W., Yao, C., Fan, J., Zhao, L., Qiu, H., Cao, X., 2022. Direct and indirect electron transfer routes of chromium(VI) reduction with different crystalline ferric oxyhydroxides in the presence of pyrogenic carbon. Environ. Sci. Technol. 56, 1724–1735.

Xue, C., Wang, C., Jiang, F., Yang, Y., Yin, H., Yi, X., Dang, Z., 2024. The effect of goethite aging on Cd adsorption: constraints of mineral condensation and surface site density. J. Hazard. Mater. 476, 134992.

Yan, W., Liu, H., Chen, R., Xie, J., Wei, Y., 2015. Dissolution and oriented aggregation: transformation from lepidorocite to goethite by the catalysis of aqueous Fe(II). RSC Adv. 5, 106396–106399.

Yan, W., Zhou, J., Liu, H., Chen, R., Zhang, Y., Wei, Y., 2016. Formation of goethite and magnetite rust via reaction with Fe(II). J. Electrochem. Soc. 163, C289–C295.

Yan, X., Zhu, M., Li, W., Peacock, C.L., Ma, J., Wen, H., Liu, F., Zhou, Z., Zhu, C., Yin, H., 2021. Cadmium isotope fractionation during adsorption and substitution with iron (oxyhydr)oxides. Environ. Sci. Technol. 55, 11601–11611.

Yang, L., Steefel, C.I., Marcus, M.A., Bargar, J.R., 2010. Kinetics of Fe(II)-catalyzed transformation of 6-line ferrihydrite under anaerobic flow conditions. Environ. Sci. Technol. 44, 5469–5475.

Yin, H., Tan, N., Liu, C., Wang, J., Liang, X., Qu, M., Feng, X., Qiu, G., Tan, W., Liu, F., 2016. The associations of heavy metals with crystalline iron oxides in the polluted soils around the mining areas in Guangdong province, China. Chemosphere 161, 181–189.

Zhao, X., Yuan, Z., Wang, S., Pan, Y., Chen, N., Tunc, A., Cheung, K., Alparov, A., Chen, W., Deevsalar, R., Lin, J., Jia, Y., 2022. Iron(II)-activated phase transformation of Cd-bearing ferrihydrite: implications for cadmium mobility and fate under anaerobic conditions. Sci. Total Environ. 848, 157719.

Zheng, X., Lu, Y., Xu, J., Geng, H., Li, Y., 2023. Assessment of heavy metals leachability characteristics and associated risk in typical acid mine drainage (AMD)-Contaminated river sediments from north China. J. Clean. Prod. 413, 137338.

Zhong, Q., Yin, L., Li, J., Feng, Y., Shen, N., Peng, B., Wang, Z., 2023. A single-stage anion exchange separation method for Cd isotopic analysis in geological and environmental samples by MC-ICP-MS. J. Anal. At. Spectrom. 38, 2291–2301.

Zhou, Z., Muehe, E.M., Tomaszewski, E.J., Lezama-Pacheco, J., Kappler, A., Byrne, J.M., 2020. Effect of natural organic matter on the fate of cadmium during microbial ferrihydrite reduction. Environ. Sci. Technol. 54, 9445–9453.